Bidirectional magnon-driven bimeron motion in ferromagnets

Xue Liang[1,*], Jin Lan[2,*], Guoping Zhao,[3] Mateusz Zelent,[4] Maciej Krawczyk[4] and Yan Zhou[1,†]

[1]*School of Science and Engineering, The Chinese University of Hong Kong, Shenzhen, Guangdong 518172, China*
[2]*Center for Joint Quantum Studies and Department of Physics, School of Science, Tianjin University, Tianjin 300354, China*
[3]*College of Physics and Electronic Engineering, Sichuan Normal University, Chengdu 610068, China*
[4]*Faculty of Physics, Adam Mickiewicz University, Uniwersytetu Poznańskiego 2, 61-614 Poznań, Poland*

As the in-plane magnetized counterparts of skyrmions in two dimensions, magnetic bimerons are swirling topological spin textures consisting of two merons. Here we theoretically and numerically investigate the dynamics of a bimeron induced by the monochromatic spin wave in a ferromagnetic thin film. The micromagnetic simulation results reveal that unlike the ferromagnetic skyrmion reported in previous studies, the bimeron can be pushed away from (or pulled towards) the wave source at the low (high) spin wave frequency. These numerical results are in line with the particle collision model formulating the interplay between the spin wave and magnetic bimeron. Our findings provide guidelines for constructing future bimeron-based spintronic devices with ultralow energy consumption.

I. INTRODUCTION

The first experimental discovery of magnetic skyrmions in 2009 [1] fascinated many physicists and has promoted the study and development of condensed matter physics and spintronics. Skyrmions are topologically nontrivial out-of-plane magnetized spin configurations with appealing properties such as good stability and nanoscale size and have been proposed as nonvolatile information carriers for the next generation of magnetic storage and computing devices [2–10]. Recently, one of their counterparts, bimerons, were discovered in chiral magnets with in-plane anisotropy [11–18], opening a new chapter in the physics of topological spin textures. The spin structure of bimerons can be symmetric or asymmetric depending on the type of the chiral Dzyaloshinskii-Moriya interaction (DMI) [19,20]. In particular, asymmetric bimerons enable some intriguing phenomena different from ordinary skyrmions, such as the formation of bimeron clusters [15] and nonreciprocal current-induced motion [16], which provide additional functional designs for future spintronic devices.

Progress in the field of topological spin textures demands the development of effective methods for triggering magnetization dynamics. The spin-polarized current is the most direct and popular way to manipulate spin textures [3,4,21–26]. Considering the fact that the inevitable Joule heating will be generated during the electron transport, however, there are still some challenges for fabricating energy-efficient magnetic devices based on spin currents. In this respect, intensive efforts have been devoted to exploring alternative approaches to control the magnetism, including the temperature gradient [27,28], gate-controlled anisotropy [29–31], and spin waves (also called magnons when quantized) [32–46]. Among them, spin waves show great potential for bringing spintronics closer to real applications in terms of energy consumption and scalable fabrication. Typically, a magnon-based current can flow through magnetic materials without the motion of electrons, which results in low power consumption due to reduced Joule heat losses [47–49]. In addition, spin waves are also allowed in both magnetic metals and insulators [50,51], opening the door for their use in various material systems. While previous studies have reported the dynamics of skyrmions induced by spin waves [34–36,38–44], the interaction between bimerons and spin waves (magnons) remains yet to be elucidated.

In this work, we demonstrate that an asymmetrical bimeron stabilized by the isotropic interfacial DMI in an in-plane ferromagnetic film can be pulled backward or pushed forward by spin waves, depending on the spin wave frequency. This bidirectional motion behavior of bimerons is different from the case of skyrmions, in which a skyrmion always moves towards the wave source in the absence of boundary effects [34,38,41]. This crucial difference between skyrmions and bimerons is attributed to the asymmetric spin configuration of bimerons and the unique characteristics of the spin wave scattering in this system.

This paper is organized as follows. Section II is devoted to the basic model for the interplay between spin waves and magnetic bimeron in the Lagrangian framework. Specifically, the wave dynamics of the spin wave is transformed to the kinematics of magnons, and the complex interplay between spin waves and bimerons is simplified to the collision scenario between magnons and bimerons. In Sec. III, the numerical results of spin wave scattering and the accompanying bimeron motion are then presented, with detailed comparisons to the particle collision calculations. A short conclusion is given in Sec. IV.

---

*These authors contributed equally to this work.
†zhouyan@cuhk.edu.cn

II. MODEL AND METHODS

A. Basic model

Consider a ferromagnetic film lying in the *x-y* plane, where the easy-axis anisotropy is along the *x* axis and the interfacial DMI arises due to the symmetry breaking in the *z* axis. The direction and magnitude of the magnetization are denoted by the unit vector **m** and the saturation magnetization M_s, respectively. The system Lagrangian [33,35,41] is given by

$$L = \int \mathcal{L} d\mathcal{V} = \int [s\mathbf{\Lambda}(\mathbf{m}) \cdot \dot{\mathbf{m}} - u(\mathbf{m})] d\mathcal{V}, \qquad (1)$$

where $\dot{\mathbf{m}} \equiv \partial_t \mathbf{m}$, $s = \mu_0 M_s / \gamma$ is the spin density, μ_0 is the vacuum permeability, γ is the gyromagnetic ratio, and $d\mathcal{V}$ is the infinitesimal volume for the integral. The first term in Eq. (1) characterizes the Wess-Zumino action for the spin precession dynamics, with $\mathbf{\Lambda}(\mathbf{m})$ being a vector potential of a magnetic monopole that satisfies $\nabla_{\mathbf{m}} \times \mathbf{\Lambda}(\mathbf{m}) = -\mathbf{m}$. The second term of Eq. (1) is the micromagnetic energy density, given by the following explicit form:

$$u(\mathbf{m}) = A(\nabla \mathbf{m})^2 + K[1 - (\mathbf{m} \cdot \hat{\mathbf{x}})^2] \\ - D\mathbf{m} \cdot [(\hat{\mathbf{z}} \times \nabla) \times \mathbf{m}], \qquad (2)$$

where *A*, *K*, and *D* are the Heisenberg exchange stiffness, magnetic anisotropy coefficient, and DMI strength, respectively. The dissipation is included in the Rayleigh function $\mathcal{R} = (\alpha/2) \int \dot{\mathbf{m}}^2 d\mathcal{V}$, where α is the Gilbert damping constant.

Invoking the Euler-Lagrange approach, Eq. (1) then yields the standard Landau-Lifshitz-Gilbert equation

$$\dot{\mathbf{m}} = -\gamma \mathbf{m} \times \mathbf{H}_{\text{eff}} + \alpha \mathbf{m} \times \dot{\mathbf{m}}, \qquad (3)$$

where $\mathbf{H}_{\text{eff}} = -(1/\mu_0 M_s) \delta u(\mathbf{m})/\delta \mathbf{m}$ is the effective field associated with various micromagnetic energies.

In this work, micromagnetic simulations are performed by using the open-access code Object Oriented Micromagnetic Framework (OOMMF) [52]. The following magnetic material parameters are adopted in simulations [3]: $M_s = 0.58$ MA m^{-1}, $A = 15$ pJ m^{-1}, $D = 3.5$ mJ m^{-2}, and $K = 0.5$ MJ m^{-3}. The protocols of spin wave generation are summarized in Appendix A. To remove abundant spin waves reflected from the film edges, an absorbing boundary condition is introduced by setting a linearly increasing damping coefficient α near the boundary region.

When time evolution is involved, the magnetization **m** in the following discussion is naturally partitioned into a slow magnetic configuration $\mathbf{m}_0$ and a fast spin wave fluctuation $\mathbf{m}'$, i.e., $\mathbf{m} = \mathbf{m}_0 + \mathbf{m}'$ [28,32]. In the small amplitude limit $|\mathbf{m}'| \ll 1$, the transverse condition $\mathbf{m}' \cdot \mathbf{m}_0 = 0$ is guaranteed. Therefore, the spin wave is generally described by $\mathbf{m}' = m_2 \hat{\mathbf{e}}_2 + m_3 \hat{\mathbf{e}}_3$ or, in a complex field, $\psi = m_2 - im_3$, where $\hat{\mathbf{e}}_{2,3}$ are two directions orthogonal to the background magnetization $\hat{\mathbf{e}}_1 = \mathbf{m}_0$. Based on such a partition scheme, we start with investigations of the spin wave in a uniform domain and the isolated magnetic bimeron before beginning studies on their interplay.

B. Spin wave in a uniform domain

In a uniform domain, $\mathbf{m}_0 = \hat{\mathbf{x}}$, the spin wave Lagrangian density is written as

$$\mathcal{L}' = \frac{is}{2} \psi^* \dot{\psi} - A\psi^* (-i\nabla + \mathbf{a}_D)^2 \psi - (K - A\mathbf{a}_D^2)\psi^*\psi, \quad (4)$$

which is derived by expanding Eq. (1) to second order in the spin wave fluctuation field ψ (see Appendix B for more details on the derivation). Here $\mathbf{a}_D = (D/2A)(\hat{\mathbf{z}} \times \mathbf{m}_0) = (D/2A)\hat{\mathbf{y}}$ is the vector potential caused by the DMI, and $\hat{\mathbf{z}}$ is the symmetry-breaking direction (or the normal to the film surface).

The variational differentiation of Eq. (4) about ψ^* yields the following Schrodinger-like equation [33,40]:

$$i\dot{\psi} = \frac{2}{s}[A(-i\nabla + \mathbf{a}_D)^2 + K - A\mathbf{a}_D^2]\psi. \qquad (5)$$

The corresponding spin wave dispersion is given by

$$\omega = \frac{2}{s}\left[A\left(\mathbf{k} + \frac{D}{2A}\hat{\mathbf{y}}\right)^2 + K - \frac{D^2}{4A}\right], \qquad (6)$$

where ω and **k** are the angular frequency and the wave vector, respectively. As a result, the group velocity is $\mathbf{v} = \partial\omega/\partial\mathbf{k} = (2/s)(2A\mathbf{k} + D\hat{\mathbf{y}})$, where the first term is the normal velocity and the second term denotes the additional velocity caused by the DMI. This is different from the case of out-of-plane easy-axis magnets, in which the DMI does not participate in the dispersion relation of spin waves excited in uniform domains [53].

The isofrequency circle determined by Eq. (6) is depicted in Fig. 1(a), where the circle's center is shifted from the origin *O* downward to point *O'* by $D/(2A)$ [37]. The directions of the wave vector **k** and the group velocity **v** are then extended from *O* and *O'* to a point on the isofrequency circle, respectively, and thus are generally noncollinear with each other. When $\mathbf{k} \parallel \hat{\mathbf{x}}$ ($k_x \neq 0$ and $k_y = 0$), the dispersion relation is symmetric with respect to the wave vector, while the group velocity is tilted upward, as shown in Fig. 1(b). On the contrary, when $\mathbf{k} \parallel \hat{\mathbf{y}}$ ($k_x = 0$ and $k_y \neq 0$), the spin wave propagation direction is collinear with the wave vector, but the magnitudes of wave vectors with opposite directions ($\mathbf{k}_y^+$ and $\mathbf{k}_y^-$) are different, as seen in Fig. 1(c). These findings are consistent with other works in which an external in-plane field is applied to force the magnetization to lie in the film plane [54,55].

Alternatively, consider the spin wave excitation in wave packet form Ψ, which maintains a relatively fixed shape during propagation and can thus be described by its centroid **r**, $\Psi(t) = \Psi[\mathbf{r}(t)]$ [41]. The spin wave Lagrangian is rewritten from Eq. (4) to (see Appendix B)

$$L' = n\left(\frac{m_{\text{sw}}}{2}\dot{\mathbf{r}}^2 - \hbar\dot{\mathbf{r}} \cdot \mathbf{a}_D\right), \qquad (7)$$

where $n = (s/2\hbar) \int \Psi\Psi^* d\mathcal{V}$ is the number of magnons contained in the spin wave packet, $m_{\text{sw}} = \hbar\partial\mathbf{k}/\partial\mathbf{v} = \hbar s/4A$ is the effective mass, and the constant terms in the Lagrangian are omitted. In this regard, the spatiotemporal evolutions of spin waves in Eq. (4) are converted to the kinematics of magnons in Eq. (7).
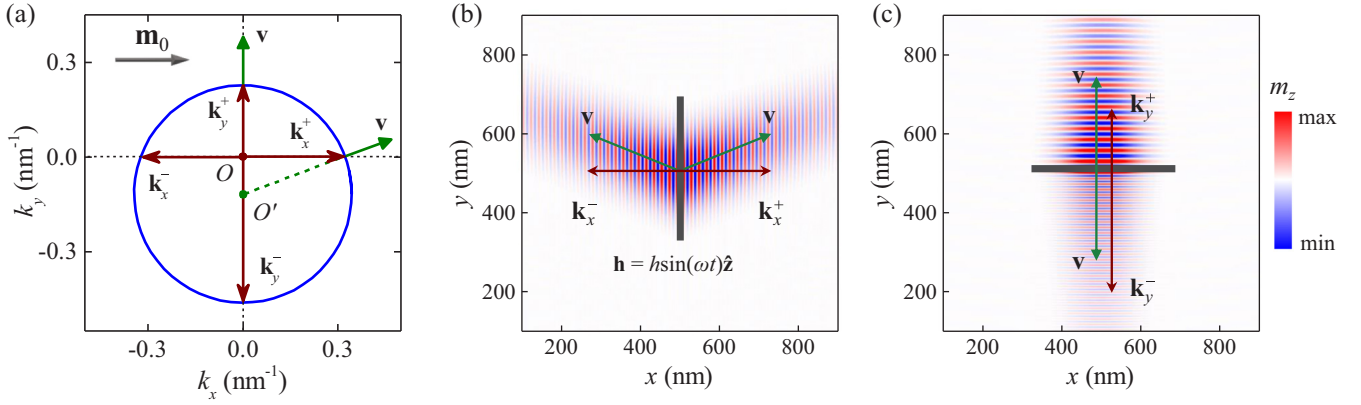
FIG. 1. Spin wave in a uniform ferromagnetic domain. (a) The isofrequency contour of the spin waves in a uniform domain $\mathbf{m}_0 = +\hat{\mathbf{x}}$. Points O and O' are the origin in k space and the center of the isofrequency circle, respectively. The red (green) arrows starting from point O (O') and ending at a point on the isofrequency circle represent the wave vector $\mathbf{k}$ (the direction of group velocity $\mathbf{v}$). (b) and (c) The spin wave beam generated by a vertical (horizontal) antenna, where $\mathbf{k}_x^{\pm}$ and $\mathbf{k}_y^{\pm}$ are the corresponding wave vectors denoted in (a).

C. Isolated magnetic bimeron

For a moderate DMI, a magnetic bimeron with a whirling magnetic structure may arise in the homogeneous domain, whose typical magnetic profile is depicted in Fig. 2(a). Similar to magnetic skyrmions, the bimeron also has a nontrivial topological structure characterized by the nonzero topological charge $Q = \pm 1$. Although the magnetic bimeron and skyrmion are topologically equivalent, the bimeron is highly asymmetric in the considered system with in-plane easy axis. This may lead to some interesting phenomena that are distinct from those of symmetric skyrmions, such as the formation of bimeron clusters and nonreciprocal current-induced motion [15,16].

According to Eq. (1), the Lagrangian of a magnetic bimeron reads

$$L_0 = \int [s\mathbf{\Lambda}(\mathbf{m}_0) \cdot \dot{\mathbf{m}}_0 - u(\mathbf{m}_0)]d\mathcal{V}. \qquad (8)$$

Since the magnetic bimeron tends to remain intact due to the topological protection and can be regarded as a rigid body, its slow motion is captured by the evolution of the bimeron centroid $\mathbf{R}$ [56], $\mathbf{m}_0(t) = \mathbf{m}_0[\mathbf{R}(t)]$. In this rigid-body approximation, the Lagrangian of the bimeron is then transformed from Eq. (8) into

$$L_0 = s\mathbf{A}_0 \cdot \dot{\mathbf{R}} - U_0, \qquad (9)$$

where $\mathbf{A}_0 = -\int \mathbf{\Lambda}(\mathbf{m}_0) \cdot \nabla\mathbf{m}_0 d\mathcal{V}$ is the vector potential accompanying bimeron motion and $U_0 = \int u(\mathbf{m}_0)d\mathcal{V}$ is the total magnetic energy of the bimeron [35,41].

D. Interplay between the spin wave and magnetic bimeron

When the spin wave travels upon a magnetic bimeron, the nonuniform magnetization of the bimeron modifies the vector potential experienced by the spin wave in two distinct aspects: (i) The original vector potential $\mathbf{a}_D$ is no longer uniform in the presence of a bimeron, and (ii) a new type of vector potential $\mathbf{a}_0 = -\mathbf{\Lambda}(\mathbf{m}_0) \cdot \nabla\mathbf{m}_0$ emerges that contains topological information about the magnetic configuration of the bimeron. After incorporating the above two ingredients into the isolated Lagrangians in Eqs. (7) and (9), the leading-order Lagrangian
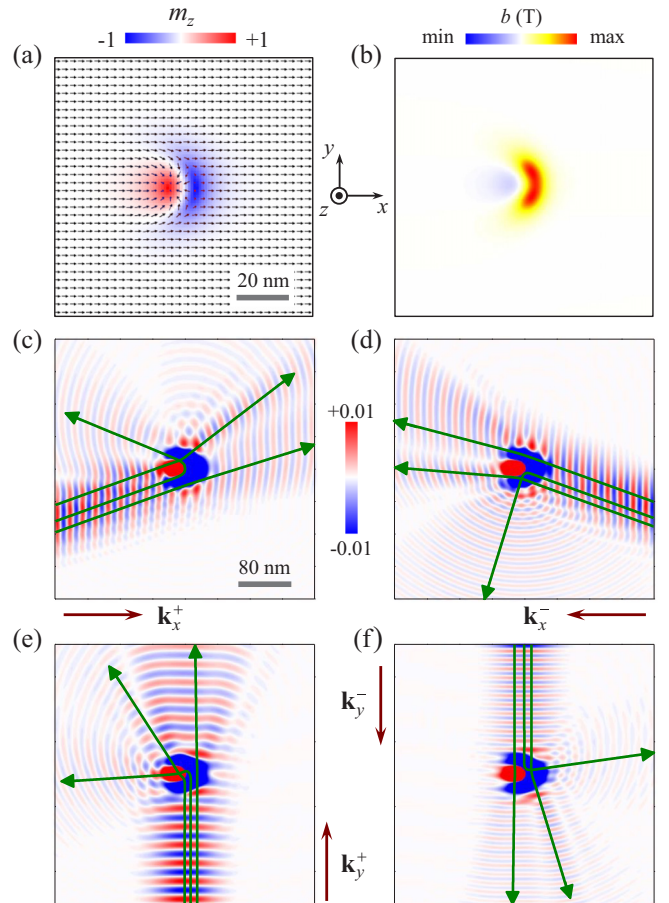
FIG. 2. Spin wave scattering by a magnetic bimeron. (a) Magnetization profile of a magnetic bimeron. The background color encodes the out-of-plane magnetization m_z, and the arrows depict the in-plane magnetization (m_x, m_y). (b) The pseudomagnetic field b induced by the magnetic bimeron. (c)–(f) The scattering of the spin wave beam generated by an antenna at one of four boundaries. The background color encodes the out-of-plane magnetization m_z, and the green lines depict the calculated magnon trajectories deflected by the pseudomagnetic field in (b).

of the system with a magnetic bimeron and spin waves (or a set of magnons) is given by (see Appendix B for detailed derivations)

$$L = s\mathbf{A}_0 \cdot \dot{\mathbf{R}} + \sum_j \left(\frac{m_{\text{sw}}}{2} \dot{\mathbf{r}}_j^2 - \hbar \dot{\mathbf{r}}_j \cdot \mathbf{a} \right), \qquad (10)$$

where $\mathbf{a} = \mathbf{a}_0 + \mathbf{a}_{\text{D}}$ is the overall vector potential mediating the interaction between the bimeron and magnons arising from the magnetic topology of the bimeron and the DMI [40,41,43]. Here $\mathbf{r}_j$ denotes the center position of the jth magnon, and the summation denotes the discretized magnons contained in the spin waves.

Application of the variational calculations to Eq. (10), i.e., $\partial_t(\partial L/\partial \dot{\mathbf{R}}) = \partial L/\partial \mathbf{R}$ and $\partial_t(\partial L/\partial \dot{\mathbf{r}}) = \partial L/\partial \mathbf{r}$, yields the kinematic equations for the bimeron and the magnon, respectively [41],

$$s\dot{\mathbf{R}} \times \mathbf{G} = -\sum_j q_0(\dot{\mathbf{r}}_j \times \mathbf{b}), \qquad (11a)$$

$$m_{\text{sw}}\ddot{\mathbf{r}}_j = -q_0 \dot{\mathbf{r}}_j \times \mathbf{b}. \qquad (11b)$$

Here the first term in Eq. (11a) is the well-known Magnus force exerted on the bimeron, with $\mathbf{G} = \nabla_{\mathbf{R}} \times \mathbf{A}_0$ being the gyrocoupling vector, $\mathbf{b} = (\hbar/q_0)\nabla \times \mathbf{a}$ is the pseudofield experienced by the magnon, and q_0 is the elementary charge. Equation (11b) indicates that the scattering process of a magnon across a bimeron is similar to the motion of a massive and charged particle in a magnetic field.

In the magnetic film of interest here, $\partial_z \mathbf{m}_0 = 0$, and thus, the pseudomagnetic field reduces to $\mathbf{b} = b\hat{\mathbf{z}}$, with $b = (\hbar/q_0)(b_0 + b_{\text{D}})$ taking the following explicit form:

$$b_0 = \mathbf{m}_0 \cdot \left(\frac{\partial \mathbf{m}_0}{\partial x} \times \frac{\partial \mathbf{m}_0}{\partial y} \right), \qquad (12a)$$

$$b_{\text{D}} = \frac{D}{2A} \nabla \cdot \mathbf{m}_0, \qquad (12b)$$

and $\mathbf{G} = (\int b_0 d\mathcal{V})\hat{\mathbf{z}} = 4\pi Q t_z \hat{\mathbf{z}}$ is related to the topological charge of the magnetic bimeron, with t_z being the thickness of the considered ferromagnetic film. As seen in Fig. 2(b), the total pseudomagnetic field b exhibits a highly asymmetric landscape due to the rotational asymmetry of the bimeron magnetization.

Integrating Eqs. (11a) and (11b) in time leads to

$$4\pi Q s t_z \hat{\mathbf{z}} \times \Delta \mathbf{R} = -m_{\text{sw}} \sum_j \Delta \mathbf{v}_j, \qquad (13)$$

where $\mathbf{v}_j \equiv \dot{\mathbf{r}}_j$ is the magnon velocity. Equation (13) is actually an alternative form of the momentum conservation, after we note that the linear momenta of the bimeron and magnon are given by $\mathbf{P} = 4\pi Q s t_z(\hat{\mathbf{z}} \times \mathbf{R})$ and $\mathbf{p} = (m_{\text{sw}}\mathbf{v} - \hbar\mathbf{a})$ [34,35,46]. Furthermore, for the case of continuous spin waves, the magnons emitted by an antenna in the time interval Δt are proportional to $v_x \Delta t$, and thus, the bimeron velocity is described by

$$\mathbf{V} \equiv \frac{\Delta \mathbf{R}}{\Delta t} \propto \frac{m_{\text{sw}} v_x}{4\pi Q s t_z} \sum_{j \in W} \hat{\mathbf{z}} \times \Delta \mathbf{v}_j, \qquad (14)$$

where W denotes the wave front parallel to the antenna.

III. RESULTS AND DISCUSSION

A. Spin wave scattering by magnetic bimerons

The scattering patterns of a spin wave beam across a magnetic bimeron are depicted in Figs. 2(c)–2(f), where the excitation antenna is deposited near one of the four film boundaries. The wave vectors of the spin wave thus take the four vectors, $\mathbf{k}_x^+$, $\mathbf{k}_x^-$, $\mathbf{k}_y^+$, and $\mathbf{k}_y^-$ in Fig. 1(a), where the propagation directions are tilted upward in Figs. 2(c) and 2(d) and the wavelength increases (decreases) in Fig. 2(e) and [Fig. 2(f)], as already elaborated in Fig. 1.

For the four scenarios shown in Figs. 2(c)–2(f), a single incident beam produces multiple scattered subbeams, revealing the complex scattering phenomena within the asymmetric bimeron. Despite the complexity, these spin wave subbeams are well reproduced by the deflection trajectories of magnons in the pseudomagnetic field, as described by Eq. (11b). In all cases, the magnons impinging directly onto the bimeron core experience the most significant deflection and give rise to the side beams that are almost perpendicular to the incident beam, while the magnons slightly deviating from the bimeron core are subject to much weaker deflection and form the main beam penetrating the bimeron. The spatially dependent deflection behaviors in Figs. 2(c)–2(f) can be attributed to the asymmetric profile of the pseudomagnetic field induced by the bimeron, as shown in Fig. 2(b). In addition, these scattering trajectories typically exhibit a counterclockwise bending since the pseudomagnetic field is predominately pointing upward therein.

B. Spin wave driven bimeron motion

To drive the bimeron more efficiently, the spin wave beam is replaced by the plane spin wave (see Appendix A) to allow more magnons to participate in the driving scenario. Here we focus on the situation in which the antenna is located on the left side of the bimeron; hence, the spin waves interacting with the bimeron propagate to the upper right direction. Figures 3(a) and 3(e) are snapshots of spin waves interacting with a magnetic bimeron at two selected frequencies, $\omega/2\pi = 300\,\text{GHz}$ and $\omega/2\pi = 100\,\text{GHz}$, respectively. For detailed comparisons and analyses, the corresponding trajectories of magnons penetrating across the pseudomagnetic fields are plotted side by side in Figs. 3(b) and 3(f).

At both frequencies in Figs. 3(a) and 3(e), a region with extremely low saturation develops on the right side of the bimeron; some bright beams with high-contrast red and blue stripes (which are traced by the yellow dashed line) accumulate above this region, and some backscattering beams arise on the left side. These scattering patterns are well reproduced by the trajectories of magnons under the pseudomagnetic field in Figs. 3(b) and 3(f), where a blank area with merely no trajectories forms and two regions featuring intersecting trajectories arise on the two sides of the bimeron.

Since the x component of the magnon velocity is proportional to the spin wave frequency while the y component remains constant for a fixed DMI, the tilting angle of incident magnons in Fig. 3(b) is smaller than that in Fig. 3(f). Considering that the fast magnons spend less penetration time in the area of pseudomagnetic field, the deflection strength of fast
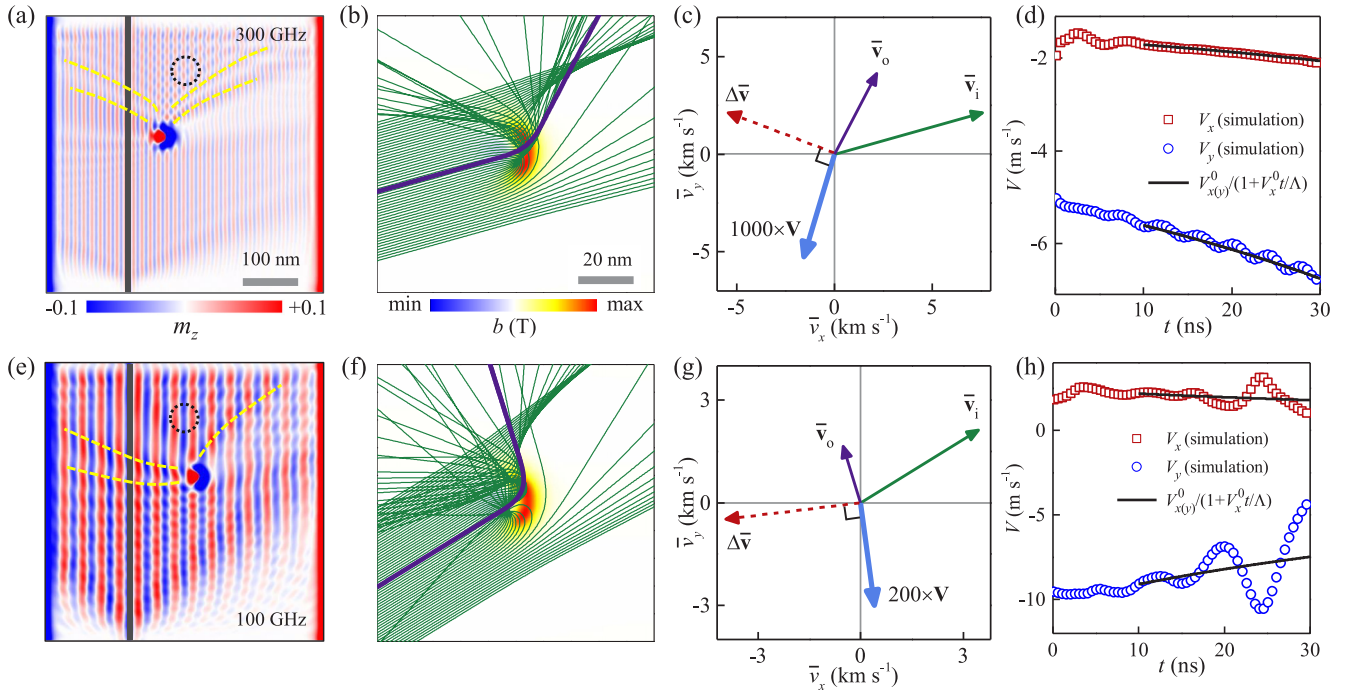
FIG. 3. Bimeron motion driven by planar spin waves with high frequency $\omega/2\pi = 300\,\text{GHz}$ in (a)–(d) and low frequency $\omega/2\pi = 100\,\text{GHz}$ in (e)–(h). (a) and (e) Snapshots of the scattering of planar spin waves by a magnetic bimeron. The background color denotes the out-of-plane magnetization m_z, the yellow dashed lines indicate the traces of bright spin wave beams, the dashed circle denotes the bimeron initial position, and the black bars depict the antennas. (b) and (f) Trajectories of magnons deflected by the pseudomagnetic field induced by a bimeron. The green lines are trajectories of each magnon, and the purple lines are the averaged trajectory of all magnons interacting with the bimeron. (c) and (g) Schematics of magnon and bimeron velocities. The green (purple) arrows denote the averaged velocities of incident (outgoing) magnons, with the red dashed arrow depicting the velocity difference between them, while the thick blue arrow represents the bimeron velocity evaluated with Eq. (14). (d) and (h) The time evolution of the velocity of the bimeron in (a) and (e), respectively. The symbols are simulation results, and the black lines are analytical calculations based on Eq. (15).

magnons is much weaker. A large fraction of fast magnons is thus able to penetrate the asymmetric landscape of the pseudomagnetic field and experience less backscattering, while the slow magnons suffer strong deflections and are mostly scattered backward. This contrasting deflection behavior at the selected frequencies is revealed by the average magnon trajectory that accounts for all magnons interacting with the magnetic bimeron, as indicated by the thick purple line pointing in the right (left) upward direction in Fig. 3(b) [Fig. 3(f)].

Following Figs. 3(a), 3(b), 3(e), and 3(f) as well as Eq. (14), the average velocity $\bar{\mathbf{v}}_{\text{i(o)}}$ of the incident and outgoing magnons, along with the velocity difference of the magnons $\Delta\bar{\mathbf{v}}$ and the bimeron velocity $\mathbf{V}$, is schematically shown in Figs. 3(c) and 3(g). For the cases with $\omega/2\pi = 300\,\text{GHz}$ and $\omega/2\pi = 100\,\text{GHz}$, the magnons acquire a negative velocity in the x direction, $\Delta\bar{v}_x < 0$, and thus, the bimeron always gains a negative velocity in the y direction, $V_y < 0$, according to Eq. (14). For high (low) frequency, the y component of the magnon velocity increases (decreases), i.e., $\Delta\bar{v}_y > 0$ ($\Delta\bar{v}_y < 0$); hence, the bimeron acquires a negative (positive) velocity in the x direction, $V_x < 0$ ($V_x > 0$). The opposite signs of $\Delta\bar{v}_y$ at $\omega/2\pi = 300\,\text{GHz}$ and $\omega/2\pi = 100\,\text{GHz}$ are attributed to different fates of fast and slow magnons traversing the pseudomagnetic field.

As the bimeron approaches (departs from) the spin wave source, the spin wave undergoes less (more) decay before

touching the bimeron, giving rise to an increase (decrease) in the bimeron velocity. More explicitly, the spin wave intensity at the bimeron center is described by $\rho = \rho_s \exp[-(X - x_s)/\Lambda]$ [46,54], where ρ_s is the spin wave intensity at the source, $\Lambda = 2Ak/s\alpha\omega$ is the spin wave attenuation length, and X and x_s are the horizontal positions of the bimeron and the wave source, respectively. The variation of the spin wave intensity is then described by $\dot{\rho}/\rho = -V_x/\Lambda$, which together with Eq. (14) leads to $\dot{V}_x/V_x = \dot{V}_y/V_y = -V_x/\Lambda$. Therefore, the time evolution of the bimeron velocity is described by [57]

$$V_{x(y)} = \frac{V_{x(y)}^0}{1 + V_x^0 t/\Lambda}, \tag{15}$$

where $V_{x(y)}^0$ is the x (y) component of the initial bimeron velocity. Here the decay length is estimated as $\Lambda = 274\,\text{nm}$ for spin wave frequency $\omega/2\pi = 100\,\text{GHz}$ and $\Lambda = 201\,\text{nm}$ for $\omega/2\pi = 300\,\text{GHz}$. Hence, for a relatively short time interval $\Delta t = 30\,\text{ns}$ and a small initial bimeron velocity $|V_x^0| \approx 2\,\text{m/s}$, the evolution of the bimeron velocity then reduces to the linear relation $V_{x(y)} = V_{x(y)}^0(1 - V_x^0 t/\Lambda)$, as verified by the monotonic variation of bimeron velocities in Figs. 3(d) and 3(h).

The velocity of bimerons driven by plane spin waves in the frequency range of $\omega/2\pi \in [100, 500]\,\text{GHz}$ is summarized in Fig. 4(a). For an intermediate spin wave frequency, the bimeron velocity also interpolates between the cases with high
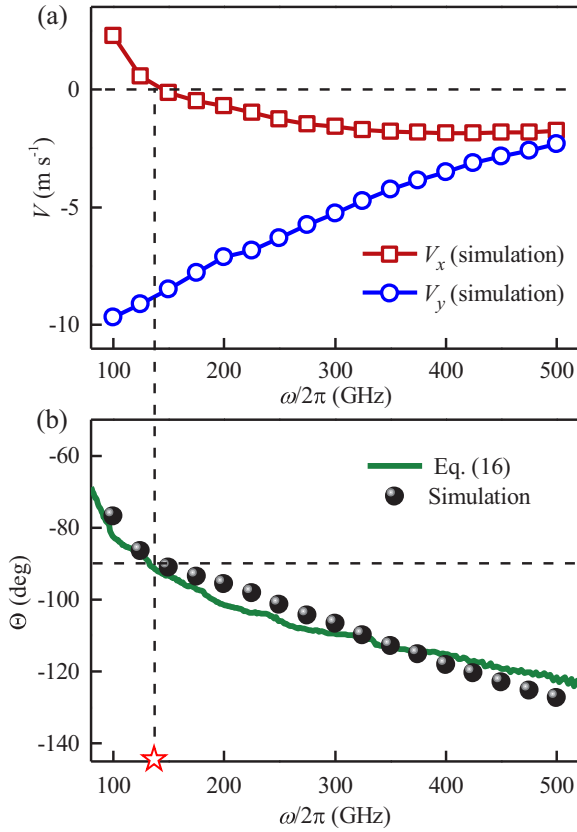
FIG. 4. (a) Spin wave driven bimeron velocity as a function of the spin wave frequency. The symbols are extracted from micromagnetic simulations, and the lines are to guide the eye. (b) The velocity angle of the bimeron as a function of the spin wave frequency. The dots show micromagnetic simulations, and the sold line shows theoretical calculations via Eq. (16). The red star marks the specific frequency $\omega/2\pi \approx 130$ GHz at which the bimeron moves parallel with the wave source.

and low frequencies due to the synergy of a moderate magnon deflection and an intermediate magnon emission rate, according to Eq. (14). Because of the crossover between positive and negative values of lateral velocity V_x, there is a specific frequency $\omega/2\pi \approx 130$ GHz for which the bimeron moves parallel to the wave source. Such a uniaxial motion behavior ($V_x = 0, V_y \neq 0$) holds promise for bimeron-based spintronic devices since the spin wave attenuation from the wave source is the same along the wave front and thus the bimeron velocity remains unaltered at different times. Meanwhile, we note that the magnitude of the bimeron velocity decreases as the spin wave frequency increases, which is attributed to the decrease in attenuation length Λ and, furthermore, the reduction in the number of magnons participating in the bimeron-magnon scattering.

The bidirectional motion feature, as illustrated in Fig. 3 by the strong (mild) deflection at low (high) frequency, is further quantitatively characterized by the angle

$$\Theta = \arctan\left(\frac{V_y}{V_x}\right) = -\frac{\sum \Delta v_j^x}{\sum \Delta v_j^y}, \quad (16)$$

where the connection to magnon velocity follows Eq. (14). As seen in Fig. 4(b), the angle extracted from micromagnetic

simulations is in exact agreement with the calculations based on the magnon-bimeron collision model, again highlighting the crucial roles of the bimeron asymmetric profile and the nonreciprocal propagation of the spin wave (magnon) in their interplay.

IV. CONCLUSION

In conclusion, we investigated the spin wave driven motion of a ferromagnetic bimeron using both the micromagnetic simulation and the simplified particle collision model. Micromagnetic simulations showed that the motion direction of the bimeron can be regulated by tuning the frequency of incident spin waves. And the particle collision model demonstrated that the bidirectional motion, i.e., the motion away from or toward the wave source, is due to the contrasting deflection angles of magnons with different incident velocities. Our results provide an energy-efficient and controllable means to manipulate magnetic bimerons.

APPENDIX A: SPIN WAVE GENERATION IN PLANAR AND BEAM FORMS

While the spin wave of frequency ω in a uniform domain $\mathbf{m}_0 = \hat{\mathbf{x}}$ is simply generated by an external magnetic field in time $\mathbf{h}(t) = h\sin(\omega t)\hat{\mathbf{z}}$, the spatial distribution of the spin wave is controlled by the spatial profile of the excitation field. Here we consider a rectangle antenna of length l_a and width w_a, with $l_a \gg w_a$ and the transverse (longitudinal) direction lying in the x' (y') axis. Hence, the magnetic field mainly varies in the transverse direction and is considered uniform in the longitudinal direction,

To generate the plane spin wave, the excitation magnetic field is spatially uniform in the whole antenna,

$$h = h_0 \Theta_H\left(\frac{l_a}{2} - |x' - x_c'|\right)\Theta_H\left(\frac{w_a}{2} - |y' - y_c'|\right), \quad (A1)$$

where h_0 is the amplitude of the excitation field, (x_c', y_c') is the central point of the antenna, and Θ_H is the Heaviside step function. Meanwhile, to generate a spin wave beam, the magnetic field takes a Gaussian-type profile along the transverse

direction of the antenna [55,58],

$$h = h_0 \exp\left[-\frac{(x' - x'_c)^2}{2\sigma^2}\right] \Theta_H\left(\frac{l_a}{2} - |x' - x'_c|\right)$$
$$\times \; \Theta_H\left(\frac{w_a}{2} - |y' - y'_c|\right), \quad (A2)$$

where σ characterizes the Gauss distribution width.

APPENDIX B: DERIVATIONS OF THE KINEMATIC EQUATIONS

In the linear spin wave regime, the total magnetization **m** can be divided into a slow magnetic texture (bimeron) $\mathbf{m}_0$ and a fast spin wave fluctuation $\mathbf{m}'$, $\mathbf{m} = \mathbf{m}_0 + \mathbf{m}'$. Following the transverse condition $\mathbf{m}_0 \cdot \mathbf{m}' = 0$, the local spin always precesses about its original equilibrium orientation with a small amplitude. Hence, defining local coordinates $\{\mathbf{e}_1, \mathbf{e}_2, \mathbf{e}_3\}$, with $\mathbf{e}_1 = \mathbf{m}_0$, the total magnetization is given by $\mathbf{m} = \mathbf{m}_0 + m_2\mathbf{e}_2 + m_3\mathbf{e}_3$, with $m_{2,3} \ll 1$. For convenience, the spin wave can be alternatively written in a complex field, $\psi = m_2 - im_3$.

Making use of the above partition scheme, the magnetic energy in Eq. (2) is expanded as

$$u_A = A(\boldsymbol{\nabla}\mathbf{m}_0)^2 + A(\boldsymbol{\nabla}\psi^* \cdot \boldsymbol{\nabla}\psi)$$
$$- iA[(\psi\boldsymbol{\nabla}\psi^* - \psi^*\boldsymbol{\nabla}\psi) \cdot \boldsymbol{\nabla}]\mathbf{m}_0 \cdot \boldsymbol{\Lambda}(\mathbf{m}_0), \quad (B1)$$

$$u_K = K[1 - (\mathbf{m}_0 \cdot \hat{\mathbf{x}})^2] + K\psi^*\psi, \quad (B2)$$

$$u_D = - D\mathbf{m}_0 \cdot [(\hat{\mathbf{z}} \times \boldsymbol{\nabla}) \times \mathbf{m}_0]$$
$$- (iD/2)(\psi\boldsymbol{\nabla}\psi^* - \psi^*\boldsymbol{\nabla}\psi) \cdot (\mathbf{m}_0 \times \hat{\mathbf{z}}), \quad (B3)$$

where only zeroth- and second-order terms in spin wave fluctuation are kept. Similarly, the Lagrangian density in Eq. (1) is then divided into the following two parts [41]:

$$\mathcal{L} = \mathcal{L}_0 + \mathcal{L}' = [s\boldsymbol{\Lambda}(\mathbf{m}_0) \cdot \dot{\mathbf{m}}_0 - u(\mathbf{m}_0)]$$
$$+ \left[\frac{is}{2}\psi^*\dot{\psi} - A\boldsymbol{\nabla}\psi^* \cdot \boldsymbol{\nabla}\psi \right.$$
$$\left. - K\psi^*\psi - iA(\psi\boldsymbol{\nabla}\psi^* - \psi^*\boldsymbol{\nabla}\psi) \cdot \mathbf{a}\right], \quad (B4)$$

where $\mathcal{L}_0$ and $\mathcal{L}'$ are the Lagrangian densities of the magnetic bimeron and spin waves. As seen in Eq. (B4), the interaction between the magnetic texture and spin waves is mediated by the minimal coupling between the spin wave flux $\psi\boldsymbol{\nabla}\psi^* - \psi^*\boldsymbol{\nabla}\psi$ and the vector potential **a**, originating

from the second expansion of the magnetic energy in Eq. (2). Here the vector potential $\mathbf{a} = \mathbf{a}_0 + \mathbf{a}_D$ consists of two parts, which are $\mathbf{a}_0 = -\boldsymbol{\Lambda}(\mathbf{m}_0) \cdot \boldsymbol{\nabla}\mathbf{m}_0$ from the magnetic topology and $\mathbf{a}_D = (D/2A)(\hat{\mathbf{z}} \times \mathbf{m}_0)$ from the DMI.

The slow motion of a magnetic texture is captured by the evolution of its central position **R**; thus, $\mathbf{m}_0(t) \equiv \mathbf{m}_0[\mathbf{R}(t)]$. By virtue of the relation $\dot{\mathbf{m}}_0 = -(\dot{\mathbf{R}} \cdot \boldsymbol{\nabla})\mathbf{m}_0$, the magnetic texture Lagrangian is then transformed to

$$L_0 = \int [-s\boldsymbol{\Lambda}(\mathbf{m}_0) \cdot (\dot{\mathbf{R}} \cdot \boldsymbol{\nabla})\mathbf{m}_0 - u(\mathbf{m}_0)]d\mathcal{V}$$
$$= s\mathbf{A}_0 \cdot \dot{\mathbf{R}} - U_0, \quad (B5)$$

where $\mathbf{A}_0 = -\int \boldsymbol{\Lambda}(\mathbf{m}_0) \cdot \boldsymbol{\nabla}\mathbf{m}_0 d\mathcal{V}$ and $U_0 = \int u(\mathbf{m}_0)d\mathcal{V}$ are the vector and scalar potentials for the magnetic texture.

Meanwhile, it is instructive to construct a spin wave packet Ψ that narrowly spans both real and reciprocal spaces and evolves solely in parametric space $\{\mathbf{r}, \mathbf{k}\}$, with **r** and **k** being the central position and wave vector, i.e., $\Psi(t) \equiv \Psi[\mathbf{r}(t), \mathbf{k}(t)]$. Following the eikonal equation in optics [59,60], as well as the semiclassical approach in quantum mechanics [61], the spin wave Lagrangian induced by one spin wave packet is transformed into [41]

$$L' = \int \left[\frac{s}{2}\mathbf{k} \cdot \dot{\mathbf{r}} - (A\mathbf{k}^2 + K + 2A\mathbf{k} \cdot \mathbf{a})\right]\Psi^*\Psi d\mathcal{V}$$
$$= \frac{2\hbar n}{s}\left[\frac{s}{2}(\mathbf{q} - \mathbf{a}) \cdot \dot{\mathbf{r}} - (A\mathbf{q}^2 + K - A\mathbf{a}^2)\right], \quad (B6)$$

where $\mathbf{q} = \mathbf{k} + \mathbf{a}$ is the canonical momentum and n is the magnon number of the localized spin wave packet with $n = (s/2\hbar)\int \Psi^*\Psi d\mathcal{V}$. The functional variation about **q** leads to $\dot{\mathbf{r}} = (4A/s)\mathbf{q}$ or $\hbar\mathbf{q} = m_{sw}\dot{\mathbf{r}}$, with $m_{sw} = \hbar s/4A$. Substituting **q** back into Eq. (B6) then yields Eq. (7) in the main text. Furthermore, considering the simultaneous presence of multiple spin wave packets each with a single magnon $n = 1$, the spin wave Lagrangian is then transformed into

$$L' = \sum_j \left(\frac{m_{sw}}{2}\dot{\mathbf{r}}_j^2 - \hbar\dot{\mathbf{r}}_j \cdot \mathbf{a}\right), \quad (B7)$$

where $\mathbf{r}_j$ is the position of the jth magnon (spin wave packet) and the terms that do not change with time are neglected.

Combining the magnetic texture Lagrangian in Eq. (B5) and the spin wave Lagrangian in Eq. (B7), the system Lagrangian is then recast from Eq. (B4) into Eq. (10) in the main text, which describes the kinematics of bimerons and magnons.

[1] S. Mühlbauer, B. Binz, F. Jonietz, C. Pfleiderer, A. Rosch, A. Neubauer, R. Georgii, and P. Böni, Science **323**, 915 (2009).

[2] A. Fert, V. Cros, and J. Sampaio, Nat. Nanotechnol. **8**, 152 (2013).

[3] J. Sampaio, V. Cros, S. Rohart, A. Thiaville, and A. Fert, Nat. Nanotechnol. **8**, 839 (2013).

[4] R. Tomasello, E. Martinez, R. Zivieri, L. Torres, M. Carpentieri, and G. Finocchio, Sci. Rep. **4**, 6784 (2014).

[5] X. Zhang, Y. Zhou, K. M. Song, T.-E. Park, J. Xia, M. Ezawa, X. Liu, W. Zhao, G. Zhao, and S. Woo, J. Phys.: Condens. Matter **32**, 143001 (2020).

[6] G. Finocchio, F. Büttner, R. Tomasello, M. Carpentieri, and M. Kläui, J. Phys. D **49**, 423001 (2016).

[7] A. Fert, N. Reyren, and V. Cros, Nat. Rev. Mater. **2**, 17031 (2017).

[8] Y. Zhou, Natl. Sci. Rev. **6**, 210 (2019).

[9] B. Göbel, I. Mertig, and O. A. Tretiakov, Phys. Rep. **895**, 1 (2021).

[10] S. Li, W. Kang, X. Zhang, T. Nie, Y. Zhou, K. L. Wang, and W. Zhao, Mater. Horiz. **8**, 854 (2021).

[11] B. Göbel, A. Mook, J. Henk, I. Mertig, and O. A. Tretiakov, Phys. Rev. B **99**, 060407(R) (2019).

[12] S. K. Kim, Phys. Rev. B **99**, 224406 (2019).

[13] X. Yu, W. Koshibae, Y. Tokunaga, K. Shibata, Y. Taguchi, N. Nagaosa, and Y. Tokura, Nature (London) **564**, 95 (2018).

[14] N. Gao, S.-G. Je, M.-Y. Im, J. W. Choi, M. Yang, Q. Li, T. Y. Wang, S. Lee, H.-S. Han, K.-S. Lee, W. Chao, C. Hwang, J. Li, and Z. Q. Qiu, Nat. Commun. **10**, 5603 (2019).

[15] X. Li, L. Shen, Y. Bai, J. Wang, X. Zhang, J. Xia, M. Ezawa, O. A. Tretiakov, X. Xu, M. Mruczkiewicz, M. Krawczyk, Y. Xu, R. F. L. Evans, R. W. Chantrell, and Y. Zhou, npj Comput. Mater. **6**, 169 (2020).

[16] L. Shen, J. Xia, Z. Chen, X. Li, X. Zhang, O. A. Tretiakov, Q. Shao, G. Zhao, X. Liu, M. Ezawa, and Y. Zhou, Phys. Rev. B **105**, 014422 (2022).

[17] K. Ohara, X. Zhang, Y. Chen, S. Kato, J. Xia, M. Ezawa, O. A. Tretiakov, Z. Hou, Y. Zhou, G. Zhao, J. Yang, and X. Liu, Nano Lett. **22**, 8559 (2022).

[18] S. Bhowal and N. A. Spaldin, Phys. Rev. Lett. **128**, 227204 (2022).

[19] I. Dzyaloshinsky, J. Phys. Chem. Solids **4**, 241 (1958).

[20] T. Moriya, Phys. Rev. **120**, 91 (1960).

[21] F. Jonietz, S. Mühlbauer, C. Pfleiderer, A. Neubauer, W. Münzer, A. Bauer, T. Adams, R. Georgii, P. Böni, R. A. Duine, K. Everschor, M. Garst, and A. Rosch, Science **330**, 1648 (2010).

[22] S. Woo, K. Litzius, B. Krüger, M.-Y. Im, L. Caretta, K. Richter, M. Mann, A. Krone, R. M. Reeve, M. Weigand, P. Agrawal, I. Lemesh, M.-A. Mawass, P. Fischer, M. Kläui, and G. S. D. Beach, Nat. Mater. **15**, 501 (2016).

[23] J. Tang, Y. Wu, W. Wang, L. Kong, B. Lv, W. Wei, J. Zang, M. Tian, and H. Du, Nat. Nanotechnol. **16**, 1086 (2021).

[24] T. Dohi, S. DuttaGupta, S. Fukami, and H. Ohno, Nat. Commun. **10**, 5153 (2019).

[25] S. Vélez, S. Ruiz-Gómez, J. Schaab, E. Gradauskaite, M. S. Wörnle, P. Welter, B. J. Jacot, C. L. Degen, M. Trassin, M. Fiebig, and P. Gambardella, Nat. Nanotechnol. **17**, 834 (2022).

[26] W. Wang, D. Song, W. Wei, P. Nan, S. Zhang, B. Ge, M. Tian, J. Zang, and H. Du, Nat. Commun. **13**, 1593 (2022).

[27] L. Kong and J. Zang, Phys. Rev. Lett. **111**, 067203 (2013).

[28] S.-Z. Lin, C. D. Batista, C. Reichhardt, and A. Saxena, Phys. Rev. Lett. **112**, 187203 (2014).

[29] X. Wang, W. L. Gan, J. Martinez, F. N. Tan, M. Jalil, and W. S. Lew, Nanoscale **10**, 733 (2018).

[30] L. Shen, J. Xia, G. Zhao, X. Zhang, M. Ezawa, O. A. Tretiakov, X. Liu, and Y. Zhou, Phys. Rev. B **98**, 134448 (2018).

[31] Y. Liu, N. Lei, C. Wang, X. Zhang, W. Kang, D. Zhu, Y. Zhou, X. Liu, Y. Zhang, and W. Zhao, Phys. Rev. Appl. **11**, 014004 (2019).

[32] P. Yan, X. S. Wang, and X. R. Wang, Phys. Rev. Lett. **107**, 177207 (2011).

[33] K. A. van Hoogdalem, Y. Tserkovnyak, and D. Loss, Phys. Rev. B **87**, 024402 (2013).

[34] J. Iwasaki, A. J. Beekman, and N. Nagaosa, Phys. Rev. B **89**, 064412 (2014).

[35] C. Schütte and M. Garst, Phys. Rev. B **90**, 094423 (2014).

[36] Y.-T. Oh, H. Lee, J.-H. Park, and J. H. Han, Phys. Rev. B **91**, 104435 (2015).

[37] W. Yu, J. Lan, R. Wu, and J. Xiao, Phys. Rev. B **94**, 140410(R) (2016).

[38] X. Zhang, J. Müller, J. Xia, M. Garst, X. Liu, and Y. Zhou, New J. Phys. **19**, 065001 (2017).

[39] C. Psaroudaki and D. Loss, Phys. Rev. Lett. **120**, 237203 (2018).

[40] S. K. Kim, K. Nakata, D. Loss, and Y. Tserkovnyak, Phys. Rev. Lett. **122**, 057204 (2019).

[41] J. Lan and J. Xiao, Phys. Rev. B **103**, 054428 (2021).

[42] Z. Jin, C. Y. Meng, T. T. Liu, D. Y. Chen, Z. Fan, M. Zeng, X. B. Lu, X. S. Gao, M. H. Qin, and J.-M. Liu, Phys. Rev. B **104**, 054419 (2021).

[43] Y. Liu, T. T. Liu, Z. Jin, Z. P. Hou, D. Y. Chen, Z. Fan, M. Zeng, X. B. Lu, X. S. Gao, M. H. Qin, and J.-M. Liu, Phys. Rev. B **106**, 064424 (2022).

[44] M. Vogel, B. Zimmermann, J. Wild, F. Schwarzhuber, C. Mewes, T. Mewes, J. Zweck, and C. H. Back, Phys. Rev. B **107**, L100409 (2023).

[45] Z. Zhang, K. Lin, Y. Zhang, A. Bournel, K. Xia, M. Kläui, and W. Zhao, Sci. Adv. **9**, eade7439 (2023).

[46] W. Wang, M. Albert, M. Beg, M.-A. Bisotti, D. Chernyshenko, D. Cortés-Ortuño, I. Hawke, and H. Fangohr, Phys. Rev. Lett. **114**, 087203 (2015).

[47] B. Lenk, H. Ulrichs, F. Garbs, and M. Münzenberg, Phys. Rep. **507**, 107 (2011).

[48] A. V. Chumak, V. I. Vasyuchka, A. A. Serga, and B. Hillebrands, Nat. Phys. **11**, 453 (2015).

[49] A. Haldar, D. Kumar, and A. O. Adeyeye, Nat. Nanotechnol. **11**, 437 (2016).

[50] V. Cherepanov, I. Kolokolov, and V. L'vov, Phys. Rep. **229**, 81 (1993).

[51] A. Serga, A. Chumak, and B. Hillebrands, J. Phys. D **43**, 264002 (2010).

[52] M. J. Donahue and M. Donahue, *OOMMF User's Guide, Version 1.0* (National Institute of Standards and Technology, Gaithersburg, MD, 1999).

[53] F. Garcia-Sanchez, P. Borys, A. Vansteenkiste, J.-V. Kim, and R. L. Stamps, Phys. Rev. B **89**, 224408 (2014).

[54] J.-H. Moon, S.-M. Seo, K.-J. Lee, K.-W. Kim, J. Ryu, H.-W. Lee, R. D. McMichael, and M. D. Stiles, Phys. Rev. B **88**, 184404 (2013).

[55] Z. Wang, B. Zhang, Y. Cao, and P. Yan, Phys. Rev. Appl. **10**, 054018 (2018).

[56] S. Komineas and N. Papanicolaou, Phys. Rev. B **92**, 064412 (2015).

[57] J. Lan and J. Xiao, Phys. Rev. B **106**, L020404 (2022).

[58] P. Gruszecki, Y. S. Dadoenkova, N. N. Dadoenkova, I. L. Lyubchanskii, J. Romero-Vivas, K. Y. Guslienko, and M. Krawczyk, Phys. Rev. B **92**, 054427 (2015).

[59] L. D. Landau and E. M. Lifshitz, *The Classical Theory of Fields*, 4th ed. (Butterworth-Heinemann, London, 1975).

[60] M. Born and E. Wolf, *Principles of Optics*, 7th ed., 60th anniversary ed. (Cambridge University Press, Cambridge, 2019).

[61] G. Sundaram and Q. Niu, Phys. Rev. B **59**, 14915 (1999).